# Structural Insights into Conformational Stability of Wild-Type and Mutant $\beta_1$-Adrenergic Receptor

Gouthaman S. Balaraman, Supriyo Bhattacharya, and Nagarajan Vaidehi*
Division of Immunology, Beckman Research Institute of the City of Hope, Duarte, California

ABSTRACT Recent experiments to derive a thermally stable mutant of turkey beta-1-adrenergic receptor ($\beta_1$AR) have shown that a combination of six single point mutations resulted in a 20°C increase in thermal stability in mutant $\beta_1$AR. Here we have used the all-atom force-field energy function to calculate a stability score to detect stabilizing point mutations in G-protein coupled receptors. The calculated stability score shows good correlation with the measured thermal stability for 76 single point mutations and 22 multiple mutants in $\beta_1$AR. We have demonstrated that conformational sampling of the receptor for various mutants improve the prediction of thermal stability by 50%. Point mutations Y227A$^{5.58}$, V230A$^{5.61}$, and F338M$^{7.48}$ in the thermally stable mutant m23-$\beta_1$AR stabilizes key microdomains of the receptor in the inactive conformation. The Y227A$^{5.58}$ and V230A$^{5.61}$ mutations stabilize the ionic lock between R139$^{3.50}$ on transmembrane helix3 and E285$^{6.30}$ on transmembrane helix6. The mutation F338M$^{7.48}$ on TM7 alters the interaction of the conserved motif NPxxY(x)$_{5,6}$F with helix8 and hence modulates the interaction of TM2-TM7-helix8 microdomain. The D186-R317 salt bridge (in extracellular loops 2 and 3) is stabilized in the cyanopindolol-bound wild-type $\beta_1$AR, whereas the salt bridge between D184-R317 is preferred in the mutant m23. We propose that this could be the surrogate to a similar salt bridge found between the extracellular loop 2 and TM7 in $\beta_2$AR reported recently. We show that the binding energy difference between the inactive and active states is less in m23 compared to the wild-type, which explains the activation of m23 at higher norepinephrine concentration compared to the wild-type. Results from this work throw light into the mechanism behind stabilizing mutations. The computational scheme proposed in this work could be used to design stabilizing mutations for other G-protein coupled receptors.

## INTRODUCTION

Obtaining three-dimensional structural information for membrane-bound G-protein coupled receptors (GPCRs) is of utmost value in designing drugs. Challenges such as obtaining sufficient quantity of the protein and stabilizing purified proteins in detergents have been overcome during the past decade, leading to the recent surge in GPCR structures (1,2). The structures of $\beta$-adrenergic receptors have been solved by attaching an antibody (3), or the T4L lysozyme in the intracellular loop (4), or by deriving thermally stable mutants that are stable in detergents (5). Serrano-Vega et al. (6) derived thermally stable mutant of turkey $\beta_1$AR with six mutations, from several stabilizing single point mutations, for which Warne et al. (5) have obtained the crystal structure. This mutant was found to be more stable in detergents than the corresponding wild-type receptor, and also mutations that increase the thermal stability of the receptor were required for obtaining a high-resolution crystal structure of $\beta_1$AR. Understanding of the mutant behavior and the origin of the stability of the mutants would allow us to incorporate these principles into a computational design algorithm, which can then be used in conjunction with experiments to design mutants for other class-A GPCRs in protein purification and biophysical experiments.

In the thermal stability measurement experiments performed by Serrano-Vega et al. (6), single point mutations of 318 residues, mostly in the transmembrane (TM) region of a truncated version of the turkey $\beta_1$AR containing residues 34–424 (represented as $\beta_1AR_{34\text{-}424}$), were tested for improved thermal stability with respect to the wild-type. They defined the stability quotient for the single mutants as the percent stability of the mutants after heating the receptor for 30 min at 32°C, normalized to the $\beta_1$AR wild-type values at 50%. For multiple mutants, a measure $T_m$ was defined as the temperature at which the functional binding dropped to 50% of unheated control (6). The wild-type $\beta_1$AR had an apparent $T_m$ of 32°C. To identify the mutation sites, the residue at each position was mutated to an alanine, or a leucine if an alanine was already present in that position. Eighteen single mutations that led to the best increase in thermal stability were identified. Subsequently, by combining up to a maximum of five single mutations in random, mutants were designed and tested for increased stability. Among these multiple mutants, one mutant labeled m10-8, which had the highest thermal stability and good expression level in *Escherichia coli*, was selected for further mutagenesis experiments (6). Mutations in m10-8 were modified by either adding or replacing the existing mutations with other single mutations that showed increased thermal stability. This led to engineering m23-$\beta_1$AR that was stable enough to be crystallized. The goal of our work is to understand the role of the mutations in reshaping the potential energy landscape of the $\beta_1$AR, and its relationship to the thermal stability.

Computational strategies have previously been developed and applied extensively to measure the change in protein

*Submitted January 7, 2010, and accepted for publication April 16, 2010.*

*Correspondence: nvaidehi@coh.org

Editor: Benoit Roux.



0006-3495/10/07/0568/10 $2.00

doi: 10.1016/j.bpj.2010.04.075

stability due to mutations, and to design proteins for water-soluble globular proteins (7–12). There are two important aspects to be considered for computational protein stability calculations: robust conformational sampling, and an appropriate energy function for stability measurement. The energy function is used to calculate the change in stability arising from a mutation. Conformational sampling of the protein has been shown to capture the effect of subtle structural changes caused by mutations, and to enhance the accuracy of computational predictions (13). Here we have designed a computational method suitable for identifying stabilizing mutations in membrane proteins.

In this work, we have used an all-atom force field energy function in conjunction with systematic coarse-grain conformational sampling using the LITiCon method (14,15) to study the effect of mutations on the thermal stability of $\beta_1$AR. We have calculated the stability of single point and multiple point mutants for various experimentally designed mutants of $\beta_1$AR (16). We have further analyzed the potential energy surface of the wild-type $\beta_1$AR and the most stable mutant m23-$\beta_1$AR. Although the wild-type receptor shows flexibility because of the possible degenerate energy states in the inactive conformation, this degeneracy is broken in the m23-$\beta_1$AR and one of the inactive states is favorably stabilized by the mutations. The six point mutations made in m23-$\beta_1$AR lead to stabilization of functional microdomains like the ionic lock between TM helices 3 and 6 and the aromatic interaction between the NPxxY(x)$_{5,6}$F motif on TM7 and helix8 (17). Using the LITiCon method, we have also studied the effect of agonist binding on the m23-$\beta_1$AR and the wild-type $\beta_1$AR conformations. We found that norepinephrine-bound m23-$\beta_1$AR shows smaller difference in binding energy between inactive and active state conformations compared to the wild-type $\beta_1$AR. In addition, the salt bridge network involving R317 (extracellular loop 3) and D184/D186 (extracellular loop 2) is weakened upon norepinephrine binding in both wild-type and m23-$\beta_1$AR receptors. We hypothesize that weakening of this salt bridge could represent a new activation switch in $\beta_1$AR.

## METHODS

### Packing the receptor structure in lipid bilayer

The receptor structures for the wild-type and mutant $\beta_1$AR were prepared in explicit lipid and water as follows. The three-dimensional structure of the mutant m23-$\beta_1$AR (PDB code: 2VT4) with antagonist cyanopindolol bound was used as the starting point for all the structures used in this study. This crystal structure does not have the intracellular loop 3 or the C-terminus residues beyond residue 359 resolved, and we used it as such for the computations. Appropriate residues in the m23 mutant structure were mutated using VMD 1.8 (18) to generate the wild-type, m19, and m20 mutant structures (the mutated positions and residues are shown in Table 1). Hydrogen atoms were added and lipid packing was done using VMD.

The following procedure was used for packing lipid bilayer for the wild-type, m23, m20, and m19-$\beta_1$AR mutant structures. The receptor was packed in 174 palmitoyl-oleoyl phosphatidylcholine lipid molecules, 12,571 water molecules, and sufficient $Na^+$ and $Cl^-$ ions to neutralize the system. The simulation box dimension containing the lipid membrane layer is ~80 Å in length, 80 Å in width, and 100 Å in height. The packing of the lipid bilayer and water was optimized in three stages of equilibration using NPT dynamics at 300 K and 1 atm using the NAMD (19), CHARMM22 (for proteins), and CHARMM27 (for lipids) force fields (20,21). The molecular dynamics was performed with 2-fs timestep along with SHAKE algorithm. Periodic boundary conditions were used with particle-mesh Ewald method, and a 12 Å nonbond cutoff. In the first stage, all but the lipid tail atoms were kept fixed and lipid tails were allowed to pack for 0.5 ns. This introduces disorder in the lipid tails, and prevents distorting the protein during production runs. In the second stage, the receptor was kept fixed and the whole of lipid and water was allowed to equilibrate for 0.5 ns. In the third stage, the receptor was subject to a harmonic constraint and was allowed to relax with the lipids and water. The final conformation of the receptor packed in the membrane environment was used for conformational sampling and molecular dynamics (MD) simulation.

**TABLE 1 Table of mutants, their mutations, and their melting temperatures**

| Mutant | Mutations | $T_m$(°C) |
|---|---|---|
| m19 | R68S, M90V, Y227A, V230A, F327A, F338M | 49 |
| m20 | R68S, M90V, V230A, A282L,* F327A, A334L | 49 |
| m23 | R68S, M90V, Y227A, A282L,* F327A, F338M | 52 |

*Mutation in the loop, which is missing in our model.

### Conformational sampling of the receptors using LITiCon method

We have used the LITiCon computational method (14–16) to sample the change in the receptor backbone and side-chain conformations in the TM region upon mutation in explicit lipid bilayer and water. The LITiCon method involves systematic spanning of the receptor conformations involving the helical rotations. We have performed simultaneous rotations of TM helices 1, 2, 5, and 7, where the mutations are present, and TMs 3, 5, and 6 to investigate TM3-TM6 salt bridge, over a range of −30° to 30° in increments of either 5° or 10°. For each of the rotated conformations, side chains were reassigned using SCWRL3.0 (22) and the resulting structure was energy-minimized using NAMD for 1000 steps, until the structure reaches a line-minimizer gradient bracket under 30 units. Subsequently the potential energy of the receptor was calculated, using the all-atom NAMD/CHARMM energy function. The LITiCon procedure measures the enthalpy component of the free energy for different receptor conformations, and can include the effect of explicit solvent on the receptor conformation and energy.

The potential energy surface thus calculated for the conformational ensemble of m23-$\beta_1$AR structure with and without receptor-lipid interaction is shown in Fig. S1 in the Supporting Material. As seen from these figures, the receptor-lipid interaction adds an offset to total interaction energy without affecting the qualitative features of the potential energy surface. However, it is possible that the lipid would affect the receptor potential energy if the lipid bilayer conformation is optimized in its packing for every receptor conformation sampled using MD or Monte Carlo simulations, but that is computationally formidable. As the lipid interaction did not change the qualitative nature of the receptor energy landscape, from here onwards we make an approximation and perform our LITiCon calculations in the absence of the lipids.

### Calculation of the stability score for mutants

A set of 128 receptor conformations close to the initial state was generated for the wild-type $\beta_1$AR using LITiCon, by rotating all the TM helices

by $\pm 5^{\circ}$. The bonded and nonbonded energy for each of the 128 conformations with all-atom force-field function in CHARMM22 was calculated for the wild-type receptor. Then for each of the 76 single point mutations (omitting the four different mutations on residue 282 present in the intracellular loop 3, IL3 that is not resolved in the crystal structure) and 22 multiple mutants derived by Serrano-Vega et al. (6), the 128 conformations generated for the wild-type $\beta_1$AR were mutated using SCWRL 3.0, and the atoms in the 5 Å radius from the mutated residue were minimized in potential energy using conjugate gradient minimization. At the end of this procedure, the bonded and nonbonded interaction energies for the receptor-ligand system were calculated using NAMD. Because the mutants have different numbers of atoms compared to the wild-type, we consider only the difference in the nonbond energy and torsional energy in calculating the stability difference between the wild-type and the mutants.

We have used two different energy functions to calculate the stability of the mutations, $E_{\mathrm{TM}}$ for the mutations in the TM regions that are hydrophobic, and $E_{\mathrm{loops}}$ for those in the extracellular or intracellular loops that are largely polar. The energy function is defined as

$$\begin{aligned} E_{\mathrm{loops}} = {} & E_{\mathrm{vdW}}(\mathrm{protein}-\mathrm{protein}) + E_{\mathrm{vdW}}(\mathrm{protein}-\mathrm{ligand}) \\ & + E_{\mathrm{elec}}(\mathrm{protein}-\mathrm{protein}) + E_{\mathrm{elec}}(\mathrm{protein}-\mathrm{ligand}) \\ & + E_{\mathrm{torsion}}(\mathrm{protein}) \end{aligned}$$

$$\begin{aligned} E_{\mathrm{TM}} = {} & E_{\mathrm{vdW}}(\mathrm{protein}-\mathrm{protein}) + E_{\mathrm{vdW}}(\mathrm{protein}-\mathrm{ligand}) \\ & + E_{\mathrm{torsion}}(\mathrm{protein}). \end{aligned} \quad (1)$$

The $E_{\mathrm{vdW}}$(protein-protein) and $E_{\mathrm{vdW}}$(protein-ligand) are the van der Waals (vdW) component of the protein-protein and protein-ligand interaction, respectively. $E_{\mathrm{elec}}$(protein-protein) is the electrostatic component of the protein interactions and $E_{\mathrm{elec}}$(protein-ligand) is the protein-ligand electrostatic interactions, both calculated with a constant dielectric of 40, and $E_{\mathrm{torsion}}$(protein) is the torsional component of the protein energy. Because the mutations in the TM regions are predominantly hydrophobic → hydrophobic, the use of vdW component for nonbond interaction captures the contribution to stability from hydrophobic packing, whereas the electrostatic component was found to have less effect on the change in stability. Also in the TM region, the accurate estimation of the electrostatic interaction needs to account for anisotropic dielectric environment inside the protein core. The electrostatic interaction was neglected in energy function for mutations in the TM regions to avoid false predictions arising from inaccuracies in its estimation. As the loop regions are predominantly polar, we have included electrostatic interactions as well to the energy function for mutations in the loop regions. The TM prediction by MEMBSTRUK 4.0 (23) was used to demarcate residues into TM and loop regions.

The value of the energy function mentioned above is computed for different conformations generated for each mutation. The minimum energy conformation is selected for wild-type and mutant from the ensemble, and the stability score is calculated as the difference of the minimum energy for the mutant and the wild-type:

$$\text{Stability score} = Min[E_{\mathrm{wild}}] - Min[E_{\mathrm{mutant}}]. \quad (2)$$

A positive (negative) value of the stability score implies increase (decrease) in stability. In the calculations, stability score with an absolute value less than a cutoff value of 1 kcal/mol is ignored. The stability score is an approximate measure of change in free energy induced by the mutation

$$\Delta\Delta G_{\mathrm{wild}\rightarrow\mathrm{mut}} = \left[G^{\mathrm{f}}_{\mathrm{mut}} - G^{\mathrm{f}}_{\mathrm{wild}}\right] - \left[G^{\mathrm{r}}_{\mathrm{mut}} - G^{\mathrm{r}}_{\mathrm{wild}}\right], \quad (3)$$

where the superscripts *f*/*r* represent folded/reference state free energies. Here we assume that the internal (bond, angle) energies of the reference extended state and the final folded state cancels out for both the wild-type and the mutant. Further, we have assumed that the difference in nonbonded energies for the reference extended state between the wild-type and the mutant is negligible, assuming that the side chains are fully extended.

## Details of the molecular dynamics simulations

We have also used all-atom MD simulations to study the effect of mutations on the microdomain structure and stability (17). The all-atom MD simulations were performed using receptor structure packed and equilibrated in lipid bilayer and the program NAMD. The production run for the MD simulations were done using the NPT ensemble at 1 atm and 305 K. Nonbond force cutoff of 12 Å was used with particle-mesh Ewald method for electrostatics along with SHAKE algorithm to constrain bond vibrations. The MD simulation run was done for 100 ns each for the wild-type, m23, m20, and m19 mutant structures. The RMSD in coordinates for the wild-type and m23 receptors from the MD simulation trajectories is shown in Fig. S4.

## Methods used to study norepinephrine binding to m23 and wild-type $\beta_1$AR

To study the effect of agonist binding to the wild-type and mutant m23-$\beta_1$AR receptors, we docked the norepinephrine molecule in the crystal structure of m23-$\beta_1$AR and the wild-type $\beta_1$AR using the GLIDE docking program (23). The docked pose that best satisfied the known mutation results for norepinephrine binding in $\beta$-adrenergic receptors was chosen. To calculate the ligand-stabilized conformational changes effected by norepinephrine binding, we used the LITiCon method (14–16) on both the m23-$\beta_1$AR and wild-type receptors. The TM helices 3, 5, and 6 were rotated between $-50^{\circ}$ and $+50^{\circ}$ in $10^{\circ}$ increments. In our previous studies on $\beta_2$AR (14–16), we found helices 3, 5, and 6 to undergo substantial conformational changes in the presence of norepinephrine and epinephrine, and hence we selected these helices for conformational scanning of norepinephrine-bound $\beta_1$AR. As the ligand can rearrange in the binding site in response to receptor flexibility, we redocked the ligand at every step of LITiCon using the docking program GLIDE (23). The local minima in the resulting energy landscapes were identified, clustered, and sorted by total number of interhelical hydrogen-bond (HB) and ligand-receptor HB and then by binding energy. The final ligand stabilized receptor structural model was selected based on low binding energy and a high number of HBs. We have used this method to predict the norepinephrine stabilized conformation in both m23 and wild-type $\beta_1$AR. The norepinephrine-bound state in the wild-type was validated agonist known point mutation studies in $\beta$-adrenergic receptors (24–27) (Fig. S7). This conformation is the predicted active state model for $\beta_1$AR.

# RESULTS

## Stability score predicts the thermal stability of the single mutants

We have calculated the stability score (defined in Methods) for 76 single mutants of $\beta_1$AR presented in Serrano-Vega et al. (6). To investigate the importance of conformational sampling in measuring thermal stability, the stability scores were calculated from a single starting conformation as well as an ensemble of conformations generated by LITiCon. It is seen from Fig. 1 *a* that 50% of the mutations are predicted in accordance with the experimental stability measurements, when conformational sampling is not included. Conformational sampling improves this prediction substantially to 75% as shown in Fig. 1 *b*. Some of the mutations that showed increase in thermal stability and were predicted correctly only with conformational sampling include residues at position I55$^{1.46}$, M90$^{2.53}$, G98$^{2.61}$, I129$^{3.40}$, S151, L221$^{5.52}$, and A234$^{5.65}$. Here we have used the class-A GPCR residue numbering system formulated by Ballesteros and Weinstein (28). (In this numbering system, the first

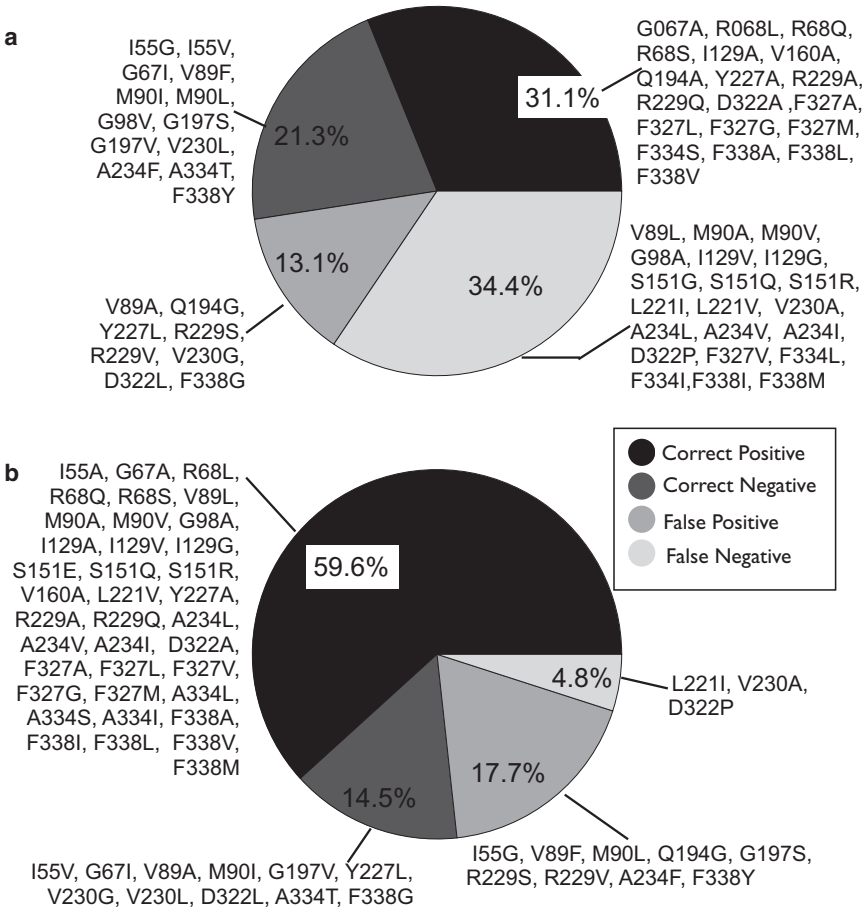


FIGURE 1 Pie chart showing the percentage correctness of predictions of the thermal stability of various single mutations using the stability score (*a*) without and (*b*) with conformational sampling. The graph classifies the predictions into correct positives, correct negatives, false positives, and false negatives.

number refers to the TM helix in which the residue is located and the second number is the position of the residue with respect to the most conserved residue on that helix among many class-A GPCRs. The most conserved residue takes the number 50 on each helix.) Barring the exception of S151, all the other mutation residue positions are in the TM region of the receptor. Thus we see that the variation/sampling in the backbone and side-chain conformations upon mutation is important for residues in the TM regions. The LITiCon method robustly samples these conformational changes upon mutation, and hence yields higher accuracy in predicting mutations.

## Stability score calculations for multiple mutants

Further, the stability score has been calculated for 22 multiple mutants formed by combining various positive single mutations that showed substantial synergistic increase in thermal stability. We have calculated the stability score for each of the 22 mutants using the procedure described in Methods. A comparison of the stability score and the $T_m$ (explained in the Introduction) from experiments by Serrano-Vega et al. (6) is shown in Fig. 2. The calculated stability score and the $T_m$ from experiments are in good agreement with an $R$-value of 0.86. The stability score correctly distinguishes the less stable mutants from the more stable ones. The error estimate in the stability score is ~1–2 kcal/mol, which accounts for the spread observed from the linear fitted line.

## Insight into thermal stabilization by mutants

To investigate the reshaping of the potential energy surface of the receptor by mutations, we performed conformational

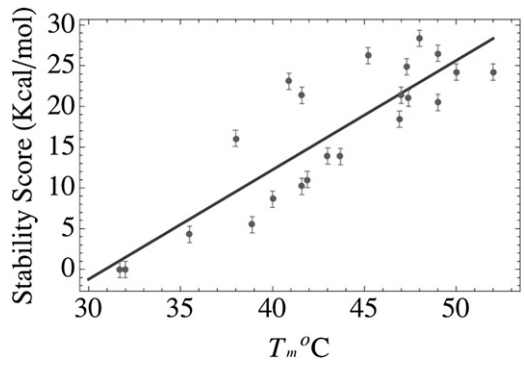


FIGURE 2 Plot of stability score versus $T_m$ for 22 mutants of $\beta_1$AR is shown with an average expected error of 1 Kcal/mol (*points*). The data is shown with a linear fitted line having $R = 0.86$.

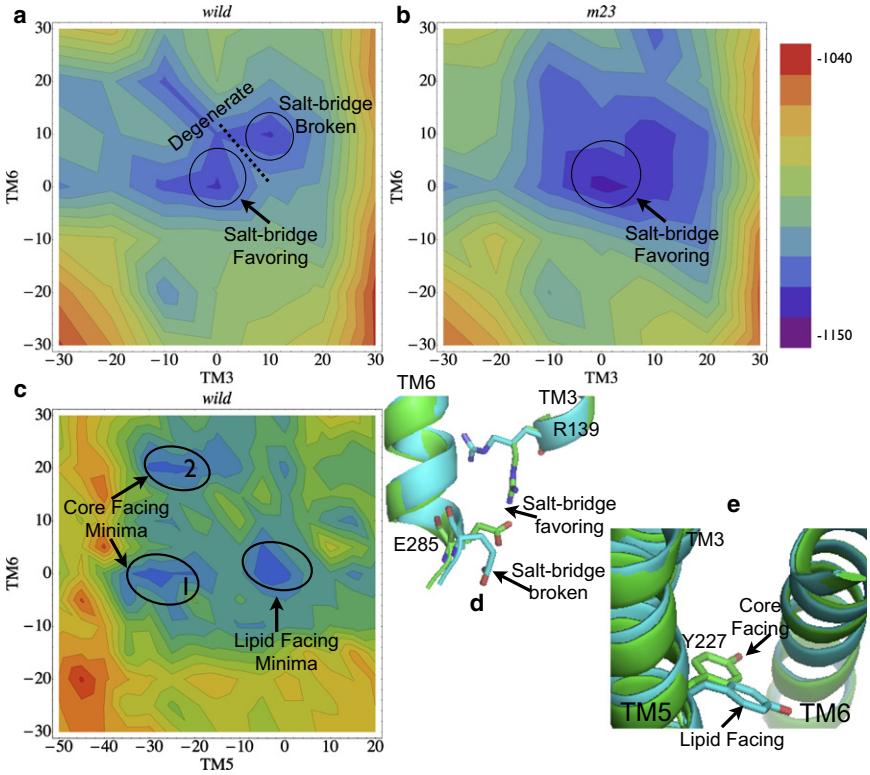


FIGURE 3 Cross section of the potential energy landscape in the TM3 and TM6 rotation angle space for (*a*) wild-type and (*b*) m23 mutant. The salt-bridge-favoring and salt-bridge-broken minima have been illustrated. (*c*) The energy landscape in the TM5-TM6 rotation space for the wild-type illustrates the lipid-facing and core-facing minima for $Y227^{5.58}$. The potential energy minimum marked "2" has the $R139^{3.50}$-$E285^{6.30}$ salt bridge broken, whereas the minimum marked "1" has $R139^{3.50}$-$E285^{6.30}$ salt bridge partially formed. (*d*) The salt-bridge-broken and salt-bridge-favoring conformations of wild-type from the two minima in panel *a* are shown. The lipid-facing and core-facing minima of the wild-type from panel *c* are shown here. Structure snapshots were generated using PyMOL from DeLano Scientific (San Francisco, CA).

sampling using LITiCon for the wild-type and three mutants m19, m20, and m23 over a wider helical rotation angle range of $-30°$ to $+30°$ in increments of $10°$. To understand the role of modulation of helical kinks in the stability of the mutant receptors we also performed an all-atom MD simulation (for 100 ns each).

## Effect of $Y227A^{5.58}$ and $V230A^{5.61}$ mutations on the receptor stability

The $Y227A^{5.58}$ mutation shows an increase of $8°C$ in the $T_m$, which is the maximum increase among all of the single mutations tested in $\beta_1AR_{34\text{-}424}$ (6). The other single mutants typically showed an increase of only 1–3°C. To understand the effect of $Y227A^{5.58}$ mutation on the receptor stability, we calculated the potential energy surface with conformational sampling using LITiCon for rotations of TM3, TM5, and TM6 that interact closely with the mutation site on TM5. Fig. 3 shows the cross section of the receptor potential energy surface for the wild-type, and the mutant m23, as a function of rotations of TM3 and TM6. The TM3-TM6 energy landscape (Fig. 3 *a*) for the wild-type exhibits two distinct potential energy minima, and the corresponding conformations are shown in Fig. 3 *d*. One of the minimum energy conformation favors the formation of salt bridge or the ionic lock between $R139^{3.50}$ and $E285^{6.30}$, and the other conformation does not. The mutant m23, on the other hand, has only one potential energy minimum in the TM3-TM6 rotation space (Fig. 3 *b*), and this corresponds to $R139^{3.50}$ and $E285^{6.30}$ in a salt-bridge-favoring orientation (not shown). We explain below how this difference in the potential energy surface for the wild-type and the mutant m23 is caused by the $Y227A^{5.58}$ mutation on TM5. $Y227^{5.58}$ in the wild-type exhibits two conformations (Fig. 3, *c* and *e*), one facing the lipids and another sandwiched between TM3 and TM6. This has also been observed in the inactive and partially active state crystal structures of rhodopsin and opsin, respectively, where the $Y223^{5.58}$ (PDB accession 1U19) faces the lipid bilayer in rhodopsin, and the $Y223^{5.58}$ is wedged between TM3 and TM6 breaking the ionic lock between $R135^{3.50}$ and $E247^{6.30}$ in the opsin structure (PDB accession 3CAP) (29).

Based on the discussion above, we hypothesize that the $Y227A^{5.58}$ mutation in m23 (and $V230A^{5.61}$ in other mutants) favors the formation of the $R139^{3.50}$-$E285^{6.30}$ ionic lock and stabilizes the inactive state conformation. This hypothesis has been further verified from the data collected using 100-ns MD simulation of the wild-type and the mutants. Fig. 4 shows the ionic-lock distance between $R139^{3.50}$ and $E285^{6.30}$ for the wild-type and m23-$\beta_1$AR. In the wild-type, a stable salt bridge is not formed between TM3 and TM6 during 100 ns of the MD simulations. This is because the $Y227^{5.58}$ flips inwards and wedges between TM3 and TM6 (data not shown) during the dynamics. In the mutant m23, although not observed in the crystal structure, a stable ionic lock is formed between $R139^{3.50}$ and $E285^{6.30}$ during the MD simulations after an initial equilibration phase. These results are similar to the observation

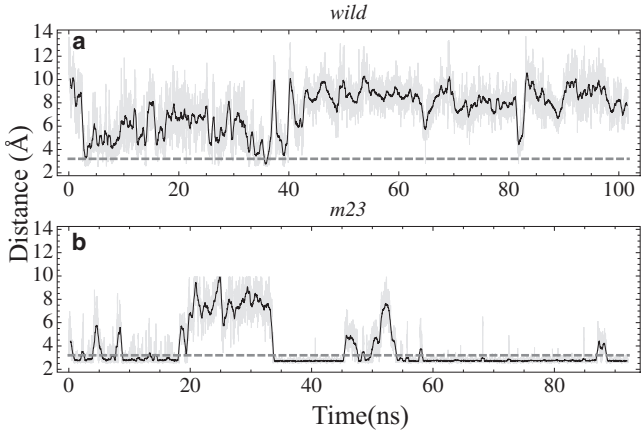


FIGURE 4 Salt-bridge N-O distance between R139$^{3.50}$ and E285$^{6.30}$ is shown for (*a*) wild-type and the (*b*) mutant m23. Ideal N-O distance of 3.2 Å is shown in shaded dashed line.

made during MD simulations of human $\beta_2$AR (30). The ionic lock between TM3 and TM6 thus contributes to the stability of the inactive state conformation of the mutant m23.

Mutant m20 has the V230A$^{5.61}$ mutation instead of Y227A$^{5.58}$ on TM5, whereas mutant m19 has both V230A$^{5.61}$ and Y227A$^{5.58}$ mutations on TM5. Both m19 and m20 mutants showed stabilization of the R139$^{3.50}$-E285$^{6.30}$ salt bridge (Fig. S2) supporting the hypothesis that Y227A$^{5.58}$ and V230A$^{5.61}$ mutations increase the stability of the inactive state by stabilizing the TM3-TM6 ionic lock therefore conferring thermal stability.

## Effect of F338M$^{7.48}$ mutation on stability

To understand the contribution of F338M$^{7.48}$ mutation to the receptor stability, we have analyzed the potential energy landscape as a function of TM1-TM2-TM7 rotation. In Fig. 5, *a* and *b*, the energy landscape of the wild-type and mutant m23 are shown as a function of TM1 and TM7 rotation angles. There are two interesting differences between the energy landscapes shown for wild-type and m23:

1. The energy minimum is deeper in the m23 by 20 kcal/mol.
2. The minimum energy for m23 is located at 10° rotation of TM7, whereas it is at −10° rotation of TM7 for the wild-type.

These observations have implication in modulating the interaction between the Y343$^{7.53}$ (part of the NPxxY(x)$_{5,6}$F motif) and F349$^{7.59}$ and hence the motion of the TM7-helix8 microdomain. Representative conformations of Y343$^{7.53}$-F349$^{7.59}$ interaction in the wild-type and m23 from MD simulations are shown in Fig. 5 *c*. In the mutant m23, the aromatic rings in Y343$^{7.53}$ and F349$^{7.59}$ are in a $\pi$-$\pi$ stacking conformation, whereas in the wild-type the $\pi$-$\pi$ stacking is broken. This is indicative of a stronger Y343$^{7.53}$-F349$^{7.59}$ interaction in m23 in comparison to the wild-type, thus

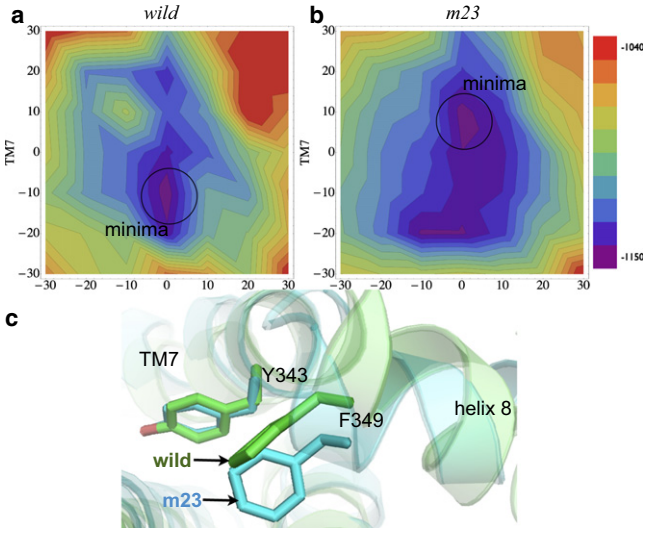


FIGURE 5 Potential energy landscape shown as a function of TM1 and TM7 rotations for (*a*) wild-type and (*b*) m23. (*c*) Representative snapshots showing conformations of Y343$^{7.53}$-F349$^{7.59}$ interaction in wild-type and m23. Structure snapshots generated using PyMOL from DeLano Scientific.

leading to an increase in thermal stability of the inactive state in m23.

The conserved NPxxY(x)$_{5,6}$F motif found in class-A GPCRs connects TM7 with helix8 in the cytoplasmic side. In rhodopsin, the Y306$^{7.53}$ forms a $\pi$-$\pi$ stacking with F313$^{7.59}$ in the inactive state, and this interaction is proposed to be broken during activation (29). Mutation results have shown that elimination of Y-F interaction in the NPxxY(x)$_{5,6}$F motif in rhodopsin leads to an increase in constitutive activity (31). Microsecond timescale simulations of rhodopsin have shown that interaction of the microdomains N302$^{7.49}$-Y306$^{7.53}$ and Y306$^{7.53}$-F313$^{7.59}$ are important in stabilizing the inactivelike conformation of rhodopsin (17). The signatures of activation revealed from their dynamical simulations include reduction in the TM7-helix8 angle from an initial near-perpendicular conformation, and an increase in the TM2-helix8 distances.

We hypothesize that the F338M$^{7.48}$ mutation directly affects the interaction of the N339$^{7.49}$-Y343$^{7.53}$ and the Y343$^{7.53}$-F349$^{7.59}$ microdomains and hence modulates the movement of TM1-TM2-TM7-helix8 bundle. The TM7-helix8 angle and TM2-helix8 distance from MD simulations is shown in Fig. 6, *a–d*. Details of the calculation of the TM7-helix8 angle are presented in the Supporting Material. We observe from the MD simulations that the TM7-helix8 angle is stabilized close to perpendicular values in the mutant m23 (Fig. 6 *b*). This correlates well with reduction in TM2-helix8 distance in m23, and is stabilized at 15.5Å (Fig. 6 *d*). The TM7-helix8 angle in the wild-type decreases below 70° (Fig. 6 *a*) and TM2 and helix8 move apart, stabilizing at 16.5 Å (Fig. 6 *c*). This correlation in the TM7-helix8 bend with TM2-helix8 distance is similar to the observations made from MD simulations of rhodopsin (17). Thus, m23

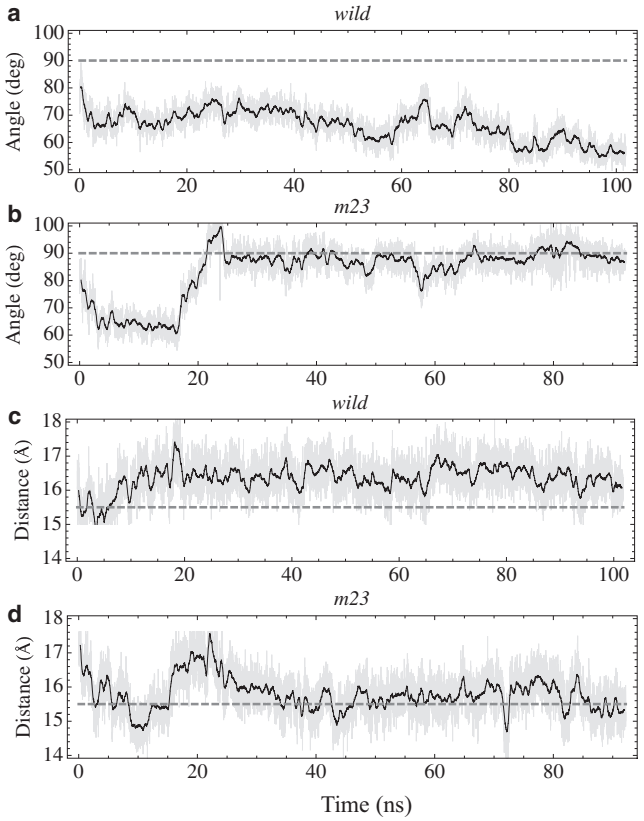


FIGURE 6 TM7-helix8 bend-angle in (*a*) wild-type and (*b*) mutant m23 as a function of time. The shaded dashed line marks the perpendicular angle. The TM2-helix8 intracellular distance measured as the $C_\alpha$-$C_\alpha$ distance between T76$^{2.39}$-A352$^{7.62}$ for the (*c*) wild-type and (*d*) m23. The shaded dashed line marks 15.5 Å.

does not exhibit the signatures of active state in the TM2-TM7-helix8 microdomain that is otherwise seen in the wild-type. Mutant m19 (with the F338M$^{7.48}$ mutation) also showed movement in the TM7-helix8 domain similar to m23, whereas m20 (which does not have the F338M$^{7.48}$ mutation) did not (Fig. S3). This asserts the importance of F338M$^{7.48}$ in stabilizing the TM2-TM7-helix8 domain and hence inactive state in the mutants.

## Effect of other mutations on thermal stability

TM1 has the R68S$^{1.59}$ mutation that stabilizes the receptor. We speculate that R68$^{1.59}$, which, in close proximity to the carboxy terminus, makes a salt bridge with one of the acidic residues E425, E427, E460, or D461 in the carboxy terminus of the receptor that has been truncated in the thermal stabilization experiments. Truncation of the carboxy terminus for crystallization could have destabilized the salt bridge formed by R68$^{1.59}$, which is stabilized in the mutants by the R68S$^{1.59}$ mutation. The mutations M90V$^{2.53}$, F327A$^{7.37}$, and F334L$^{7.44}$ are located on TM2 and TM7, respectively. These mutations confer a stability of 1–3°C in temperature, and show an improvement in the enthalpy component in our calculations. These mutations possibly lead to better side-chain packing in the receptor, and hence contribute to an increase in stability.

## Effect of thermostable mutations on the loop conformations

In a recent work, Bokoch et al. (32) have shown that in human $\beta_2$AR, agonists, neutral antagonists, and inverse agonists stabilize different conformations of the D192-K305 salt bridge connecting extracellular loops 2 and 3. Therefore, we investigated whether a similar salt bridge could be found among the extracellular loops of $\beta_1$AR. Turkey $\beta_1$AR has an acidic residue (D322$^{7.32}$) at the homologous position of the basic residue K305$^{7.32}$ in $\beta_2$AR and hence, the salt bridge analogous to the one found in $\beta_2$AR is missing in $\beta_1$AR. However, we identified an alternate salt bridge connecting extracellular loop 2 and extracellular loop 3 involving residues D184 and R317 in the crystal structure of the m23-$\beta_1$AR. The D186 on extracellular loop 2 is also close to R317, but does not form a salt bridge. As shown in the multiple sequence alignment (Fig. S5), residues D184, D186, and R317 are conserved among $\beta_1$ receptors across different species, suggesting the importance of this salt bridge in modulating receptor functionality. During the MD simulations of wild-type $\beta_1$AR bound to cyanopindolol, the salt-bridge partner of R317 shifted from D184 to D186 and remained stable throughout the simulation (Fig. 7 *a*). In contrast, during the MD simulation of the mutant m23, two alternating salt bridge conformations, D186-R317 and D184-R317, were stabilized (Fig. 7 *b*). Interestingly, the other mutants m20 and m19 also showed a propensity to form both salt bridges during their respective MD simulations, although favoring D184-R317 over D186-R317 salt bridge. The variation in distance between the guanidinium nitrogen of R317 and carboxylic oxygen of D184 and D186 in the wild-type and m23 mutant receptors is shown in Fig. 7, *c* and *d*, respectively. During the MD simulation of wild-type receptor (Fig. 7 *c*), the D184-R317 salt bridge is disrupted within 10 ns (distance increases to 4–5 Å) and the D186-R317 salt bridge is formed in its place (distance 2.8 Å). In the m23 receptor (Fig. 7 *d*), the D184-R317 salt bridge is stable until 40 ns, when this salt bridge is disrupted and an alternate salt bridge is formed between R317 and D186. Then after 80 ns, the D186-R317 salt bridge is disrupted and the D184-R317 salt bridge is reformed. As the wild-type receptor forms D186-R317 salt bridge only in the MD simulations, we propose that the disruption of the D186-R317 salt bridge in a mutation experiment could destabilize the wild-type receptor. In the m23 mutant, because both D184-R317 and D186-R317 salt bridges are favorably formed, the effect of disrupting one of the salt bridges could be compensated for by the formation of the other salt bridge and thus lead to increased stability of the m23 mutant over wild-type $\beta_1$AR.

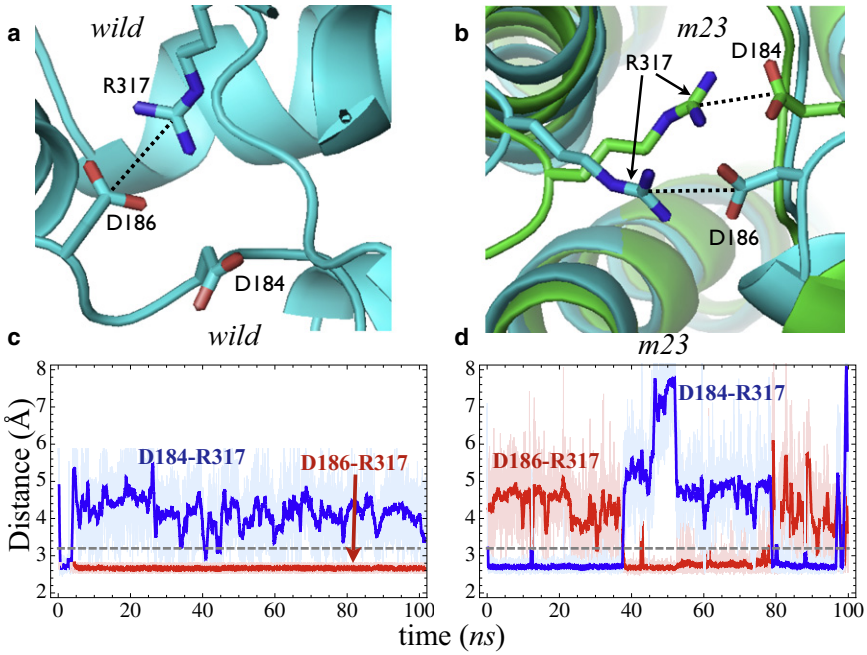


FIGURE 7 Representative snapshots of conformation of salt bridge between extracellular loop 2 and 3 (*a*) linking D186-R317 in wild-type, (*b*) and linking both D186-R317 and D184-R317 in m23. The salt-bridge N-O distance for (*c*) wild-type and (*d*) m23 is shown. The ideal N-O distance of 3.2 Å is shown in shaded dashed line.

### Effect of norepinephrine binding on the salt bridge

We calculated the probability of occurrence of the R317-D184/D186 salt bridges in the inactive and predicted norepinephrine-bound active states of both wild-type and m23 $\beta_1$AR using the side-chain reassignment program SCREAM (33). In both wild-type and m23 receptors, the side chains of R317 and D186 showed 63% and 85% reduction in salt-bridge population in the predicted active state compared to the cyanopindolol bound inactive state. In addition, in the predicted active state of the m23 mutant, the salt bridge between D184 and R317 was completely disrupted (100% reduction in salt-bridge population compared to inactive state). Thus, the predicted active state models of both wild-type and m23 $\beta_1$AR show higher propensity for breaking the R317 to D184 or D186 salt bridge compared to the inactive state. This result is similar to the observation made by Bokoch et al. (32) in $\beta_2$AR, where they used NMR experiments to show that the salt bridge between K305 and D192 in $\beta_2$AR was disrupted on binding to agonist formoterol, whereas this salt bridge was preserved in the unliganded and antagonist-bound receptors. Thus, the salt bridge involving R317 and D184/D186 in $\beta_1$AR could act as a possible conformational switch-mediating, agonist-induced $\beta_1$AR activation.

### Effect of thermal stable mutations on agonist binding on m23 mutant compared to the wild-type $\beta_1$AR

We investigated the effect of thermostable mutations on agonist binding by computing the binding energy landscapes of the agonist norepinephrine bound to the wild-type and m23 mutant of $\beta_1$AR (Fig. S6) using LITiCon method as described in Methods. Both wild-type and m23-$\beta_1$AR receptors show a wide binding energy trough near the crystal conformation and another binding-energy minimum that is predicted to be the norepinephrine-stabilized state in our calculations. The calculated binding energy of norepinephrine in the predicted active state of the wild-type $\beta_1$AR is 5 kcal/mol better than its binding energy in the inactive state, whereas the same difference in m23-$\beta_1$AR is only 0.5 kcal/mol. Thus, binding of norepinephrine to the wild-type $\beta_1$-AR shifts the inactive ↔ active equilibrium toward the active state. The m23 receptor has less constitutive activity compared to the wild-type. In addition, due to small difference in binding energy between the inactive and the active states, low concentrations of norepinephrine does not shift the equilibrium toward the active state in m23. This shows that the m23 receptor requires higher concentration of norepinephrine for receptor activation. Thus, our observations are in agreement with the results from competition binding with the antagonist dihydroalprenolol (DHA), where norepinephrine displaced radiolabeled DHA at a higher concentration in m23 compared to wild-type (6). The reason for the lower difference in binding energy between the inactive and active states in m23 is not evident from the ligand-residue interaction energies calculated for residues in the binding site (residues within 5 Å of the ligand). The difference in binding energy is possibly due to allosteric effects of the mutations in m23 that are distant from the binding cavity.

## DISCUSSION

Recent experiments (6) have demonstrated that stable mutants of certain class-A GPCRs can be engineered for biophysical studies. We have designed a computational

method using all-atom force-field energy function and LITiCon, a coarse-grained conformational sampling method, to detect stable single point mutations in GPCRs. The computational method applied to single point mutations in $\beta_1$AR showed 75% accuracy in detecting the mutations identified in the experiments. Using LITiCon and MD simulations, we have analyzed the mechanism behind stabilizing mutations. The Y227A$^{5.58}$ and V230A$^{5.61}$ mutations stabilized the receptor by increasing the propensity for salt-bridge formation between R139$^{3.50}$ on TM3 and E285$^{6.30}$ on TM6. The salt bridge between TM3 and TM6, a putative signature of the inactive state, is stabilized by these mutations and hence contributes to an increase in stability. The mutation F338M$^{7.48}$ on TM7 alters the interaction in the conserved motif NPxxY(x)$_{5,6}$F, and hence, modulates the interaction of TM2-TM7-helix8 microdomain. This modulation stabilizes the inactivelike feature of nearly perpendicular TM7-helix8 bend angle and smaller TM2-helix8 intracellular distance. From these results, we infer that the increased stability in the mutants arises due to stabilization of certain features characteristic of the inactive state found in the conserved microdomains. Stabilization of the inactive state in the mutants could be the reason for their reduced constitutive activity compared to the wild-type. As the thermal stabilization in the mutants is mediated through conserved microdomains, it was possible to transfer the thermostabilizing mutations from $\beta_1$AR to $\beta_2$AR as reported in a recent work (34). Increased propensity of the D184/D186-R317 salt bridge in the extracellular loops also enhances the stability of the inactive state in m23. However, we believe that the interhelical contacts that stabilize the inactive and active state conformations are different in peptide-binding class-A GPCRs. Therefore, the stabilizing mutations could be different in these receptors and this remains to be studied.

The LITiCon energy potential energy landscape for wild-type and the mutant differs in shape and ruggedness around the global minimum. The wild-type had nine minima in the multidimensional LITiCon energy landscape, whereas the mutants m19, m20, and m23 had four minima each and one of these minima is the DHA-stabilized inactive state. The stabilizing mutations in $\beta_1$AR alter the global energy landscape such that there are fewer preferred conformations for the mutants around the inactive state in comparison to the wild-type. Due to the presence of more minima in the wild-type than the mutants, we speculate that at elevated temperatures the wild-type receptor can sample multiple conformational states and thereby reduce the receptor population in the DHA stabilized inactive state. Hence, the wild-type receptor could exhibit reduced DHA binding activity at elevated temperatures. The mutants have fewer minima, and hence populate the DHA bound conformation with higher propensity, thereby leading to better binding to DHA at higher temperatures. However, it is not clear whether the $\beta_1$AR mutants would melt or unfold at higher temperatures than the wild-type $\beta_1$AR.

## SUPPORTING MATERIAL

Seven figures are available at http://www.biophysj.org/biophysj/supplemental/S0006-3495(10)00657-0.

G.S.B. thanks Dr. Jianping Lin for useful discussions.

The authors thank the Beckman Research Institute of the City of Hope for funding this research.

## REFERENCES

1. Blosis, T. M., and J. U. Bowie. 2009. G-protein-coupled receptors were not built in a day. *Prot. Sci.* 18:1335–1342.
2. Rosenbaum, D. M., S. G. F. Rasmussen, and B. K. Kobilka. 2009. The structure and function of G-protein-coupled receptors. *Nature*. 459:356–363.
3. Rasmussen, S. G. F., H. J. Choi, …, B. K. Kobilka. 2007. Crystal structure of the human $\beta$2 adrenergic G-protein-coupled receptor. *Nature*. 450:383–387.
4. Rosenbaum, D. M., V. Cherezov, …, B. K. Kobilka. 2007. GPCR engineering yields high-resolution structural insights into $\beta$2-adrenergic receptor function. *Science*. 318:1266–1273.
5. Warne, T., M. J. Serrano-Vega, …, G. F. Schertler. 2008. Structure of a $\beta$1-adrenergic G-protein-coupled receptor. *Nature*. 454:486–491.
6. Serrano-Vega, M. J., F. Magnani, …, C. G. Tate. 2009. Conformational thermostabilization of $\beta$1-adrenergic receptor in a detergent-resistant form. *Proc. Natl. Acad. Sci. USA*. 105:877–882.
7. Malakauskas, S. M., and S. L. Mayo. 1998. Design, structure and stability of a hyperthermophilic protein variant. *Nat. Struct. Biol.* 5:470–475.
8. Massova, I., and P. A. Kollman. 1999. Computational alanine scanning to probe protein-protein interactions: a novel approach to evaluate binding free energies. *J. Am. Chem. Soc.* 121:8133–8143.
9. Lazar, G. A., S. A. Marshall, …, J. R. Desjarlais. 2003. Designing proteins for therapeutic applications. *Curr. Opin. Struct. Biol.* 13:513–518.
10. Kuhlman, B., and D. Baker. 2004. Exploring folding free energy landscapes using computational protein design. *Curr. Opin. Struct. Biol.* 14:89–95.
11. Hellinga, H. W. 1997. Rational protein design: combining theory and experiment. *Proc. Natl. Acad. Sci. USA*. 94:10015–10017.
12. Butterfoss, G. L., and B. Kuhlman. 2006. Computer-based design of novel protein structures. *Annu. Rev. Biophys. Biomol. Struct.* 35:49–65.
13. Benedix, A., C. M. Becker, …, R. A. Böckmann. 2009. Predicting free energy changes using structural ensembles. *Nat. Methods*. 6:3–4.
14. Bhattacharya, S., S. E. Hall, …, N. Vaidehi. 2008. Ligand-stabilized conformational states of human $\beta$2 adrenergic receptor: insight into G-protein-coupled receptor activation. *Biophys. J.* 94:2027–2042.
15. Bhattacharya, S., S. E. Hall, and N. Vaidehi. 2008. Agonist-induced conformational changes in bovine rhodopsin: insight into activation of G-protein-coupled receptors. *J. Mol. Biol.* 382:539–555.
16. Bhattacharya, S., and N. Vaidehi. 2010. Computational mapping of the conformational transitions in agonist selective pathways of a G-protein coupled receptor. *J. Am. Chem. Soc.* 132:5205–5214.
17. Khelashvili, G., A. Grossfield, …, H. Weinstein. 2009. Structural and dynamic effects of cholesterol at preferred sites of interaction with rhodopsin identified from microsecond length molecular dynamics simulations. *Proteins*. 76:403–417.
18. Humphrey, W., A. Dalke, and K. Schulten. 1996. VMD: visual molecular dynamics. *J. Mol. Graph.* 14:33–38, 27–28.
19. Phillips, J. C., R. Braun, …, K. Schulten. 2005. Scalable molecular dynamics with NAMD. *J. Comput. Chem.* 26:1781–1802.
20. MacKerell, Jr., A. D., D. Bashford, …, M. Karplus. 1998. All-atom empirical potential for molecular modeling and dynamics Studies of proteins. *J. Phys. Chem. B*. 102:3586–3616.

21. Feller, S., and A. D. MacKerell. 2000. An improved empirical potential energy function for molecular simulations of phospholipids. *J. Phys. Chem. B*. 104:7510–7515.

22. Canutescu, A. A., A. A. Shelenkov, and R. L. Dunbrack, Jr. 2003. A graph-theory algorithm for rapid protein side-chain prediction. *Protein Sci.* 12:2001–2014.

23. Hall, S. E. 2005. Development of a structure prediction method for G-protein coupled receptors. PhD thesis. Caltech, Pasadena, CA.

24. Friesner, R. A., R. B. Murphy, …, D. T. Mainz. 2006. Extra precision glide: docking and scoring incorporating a model of hydrophobic enclosure for protein-ligand complexes. *J. Med. Chem.* 49:6177–6196.

25. Strader, C. D., I. S. Sigal, …, R. A. Dixon. 1988. Conserved aspartic acid residues 79 and 113 of the $\beta$-adrenergic receptor have different roles in receptor function. *J. Biol. Chem.* 263:10267–10271.

26. Liapakis, G., J. A. Ballesteros, …, J. A. Javitch. 2000. The forgotten serine. A critical role for Ser-2035.42 in ligand binding to and activation of the $\beta$2-adrenergic receptor. *J. Biol. Chem.* 275:37779–37788.

27. Wieland, K., H. M. Zuurmond, …, M. J. Lohse. 1996. Involvement of Asn-293 in stereospecific agonist recognition and in activation of the $\beta$2-adrenergic receptor. *Proc. Natl. Acad. Sci. USA*. 93:9276–9281.

28. Ballesteros, J. A., and H. Weinstein. 1995. Integrated methods for modeling G-protein coupled receptors. *Methods Neurosci.* 25:366–428.

29. Park, J. H., P. Scheerer, …, O. P. Ernst. 2008. Crystal structure of the ligand-free G-protein-coupled receptor opsin. *Nature*. 454:183–187.

30. Dror, R. O., D. H. Arlow, …, D. E. Shaw. 2009. Identification of two distinct inactive conformations of the $\beta_2$-adrenergic receptor reconciles structural and biochemical observations. *Proc. Natl. Acad. Sci. USA*. 106:4689–4694.

31. Fritze, O., S. Filipek, …, O. P. Ernst. 2003. Role of the conserved NPxxY(x)5,6F motif in the rhodopsin ground state and during activation. *Proc. Natl. Acad. Sci. USA*. 100:2290–2295.

32. Bokoch, M. P., Y. Zou, …, B. K. Kobilka. 2010. Ligand-specific regulation of the extracellular surface of a G-protein-coupled receptor. *Nature*. 463:108–112.

33. Kam, V. W. T., and W. A. Goddard, III. 2008. Flat-bottom strategy for improved accuracy in protein side-chain placements. *J. Chem. Theory Comput.* 4:2160–2169.

34. Serrano-Vega, M. J., and C. G. Tate. 2009. Transferability of thermostabilizing mutations between $\beta$-adrenergic receptors. *Mol. Membr. Biol.* 26:385–396.